Nano Research

Open Access

Research Article

Surface micro-arrays enhancing electromagnetic interference shielding of polydimethylsiloxane/multiwalled carbon nanotubes nanocomposites

Ke Jiang[1], Zhi Chen Ji[1], Yu Chen Zheng[1], Shan Huang[2] ✉, and Ming Wang[1,3] ✉

[1] *Chongqing Key Laboratory of Soft-Matter Material Manufacturing, School of Chemistry and Chemical Engineering, Southwest University, Chongqing 400715, China*
[2] *School of Mechanics, Civil Engineering and Architectures, Northwestern Polytechnical University, Xi'an 710072, China*
[3] *Jieyang Branch of Chemistry and Chemical Engineering Guangdong Laboratory (Rongjiang Laboratory), Jieyang 515200, China*

Cite this article: *Nano Research*, **2025**, *18*, 94907153. https://doi.org/10.26599/NR.2025.94907153

ABSTRACT: Herein, the electromagnetic shielding performance of surface concave-convex (SC) and zig-zag micro-arrays was studied by using a simulation prediction and a three-dimensional (3D) printing custom model. Firstly, surface stripe concave-convex (SSC) and surface cylindrical concave-convex (SCC) micro-arrays with or without zig-zag micro-arrays are designed, and their shielding performance is simulated in multi-bands (C-, X-band). The multiwalled carbon nanotubes/polydimethylsiloxane composites (MWCNT/PDMS) with different SC structures and different electrical conductivity are molded in acrylonitrile-butadiene-styrene copolymer (ABS) molds which are printed by a 3D printer. The results show that the electromagnetic interference shielding effectiveness (EMI SE) of the samples can be enhanced by constructing the SC micro-arrays with zig-zag micro-arrays, and improving with the increase of conductivity and frequency. In addition, the shielding mechanism of the SC-MWCNT/PDMS composites is investigated and discussed by an electromagnetic simulation.

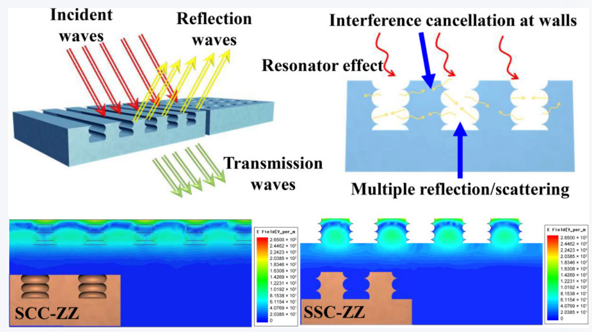

KEYWORDS: surface micro-arrays, electrical properties, electromagnetic interference (EMI) shielding, three-dimensional (3D) printing

1 Introduction

The high degree of informatization in modern society has brought great changes and convenience to people's lives. These developments are inseparable from the widespread use of microwave facilities and wireless communications, which has led to increasingly complex and serious electromagnetic interference (EMI) radiation problems. Electromagnetic pollution not only interferes with the operation of various electronic equipment but also can adversely affect human health when exposed to complex electromagnetic waves (EMWs) for a long time [1–5].

Fortunately, the propagation of electromagnetic waves can be blocked by some conductive and magnetic materials which are defined as EMI shielding materials to protect related equipment [6–8]. EMI shielding materials mainly attenuate EMW through two shielding mechanisms of surface reflection and internal absorption [9–11]. Metals are the earliest and most widely used EMI shielding materials, but problems such as high density and processing difficulties also limit the development of metal shielding materials [12–14]. Conductive polymer composites (CPCs), as excellent EMI shielding materials that are lightweight, easy to process, and cost-controllable [15–18], are increasingly accepted as having both surface reflection loss and internal absorption loss to electromagnetic waves, reducing secondary reflection pollution [19–21]. Furthermore, CPCs can be easily designed with unique structures, such as multilayered structures [22–25], porous or foamed structures [26–29], and isolated structures [30–33], to enhance EMI shielding performance with low reflections. These abundant structures are mainly to build more interfaces inside CPCs so that electromagnetic waves are reflected or scattered multiple times in the interface. As a result, the EMW energy is rapidly attenuated [34]. However, there are few studies on the

Received: November 1, 2024; **Revised:** November 21, 2024
Accepted: November 24, 2024

✉Address correspondence to Shan Huang, huangshan@nwpu.edu.cn; Ming Wang, mwang@swu.edu.cn

structure regulation on CPCs surface to obtain a better EMI shielding effect [13, 35]. Compared with the construction of internal structures, the structural design on the surface of CPCs which is relatively simple and efficient is possible to customize the required structure of the rules [35–37]. Additionally, certain materials featuring circular concave honeycomb and dot matrix structures exhibit excellent electromagnetic shielding properties. For instance, Li et al. demonstrated a dual shielding effect against both electromagnetic and acoustic waves by integrating graphene paper with artificial honeycomb panels [38]. Furthermore, Liu et al. developed a double-layer film infused with liquid metal, transforming the liquid metal from a discrete dot matrix configuration to a strip connection through a compressive strain method. The approach significantly enhanced the electromagnetic shielding performance, increasing it from 9 to 42 dB [39].

At present, three-dimensional (3D) printing technologies have become a widely used material manufacturing method due to its special manufacturing mode, which can realize the construction of diverse structures [40–43]. For example, a 3D printed structure with gradient porosity was designed based on the TiO_2-$Ti_3C_2T_x$/rGO framework, which has good electromagnetic interference shielding effectiveness (EMI SE) through improving impedance matching and multiple internal reflections of EMWs [44]. Furthermore, 3D printing can also establish asymmetrical structures for directional EMI shielding [45]. Therefore, the use of 3D printing can be used as a low-cost solution for customizable and unique structures [46, 47].

In addition, electromagnetic simulation is a method that uses numerical models to predict or verify the electromagnetic performance of actual structures by performing simulation analysis [48–50]. The use of electromagnetic simulation can guide structural design and eliminate a large number of ineffective experiments, which can greatly reduce the time and economic cost [51–53]. Furthermore, the electromagnetic simulation can simulate the change of electromagnetic field at the model, which is also a method to explore and verify the electromagnetic response mechanism of target materials [54–56]. Additionally, in the field of EMI, CPCs are mostly studied in the X-band (8.2–12.4 GHz), and there is little research on lower frequencies, such as C-band (4–8.2 GHz). However, in the current 5G era, there are numerous frequency bands within the C-band allocated for 5G signals, which underscores the importance of enhancing shielding for this frequency range. On one hand, the shielding effect of C-band EWMs is generally obtained by preparing composite materials with highly conductivity [57–60]. On the other hand, multi-component fillers are used to enhance EMI SE values in C-band via multiple synergistic effect, such as magneto–electric synergistic effect [61–63]. For example, a kind of rGO/PdNi multi-component fillers was added into poly(ethylene-co-vinyl acetate) matrix, and the EMI SE value in the C band of the samples was 30 dB because of a magneto–electric synergistic effect [64]. However, the structural design of CPCs, especially surface structure, is rarely reported to improve the EMI shielding performance of low-frequency electromagnetic waves.

So far, research on enhancing the EMI shielding performance of CPCs through surface structure design is still relatively scarce. In this study, we propose a simple structural design for the composite material surface and validate its effect on EMI shielding enhancement through a combination of simulations and experiments. This work provides a solid foundation for the further development of surface structures designed to enhance EMI shielding performance. Specifically, a simulation and experimental study are carried to investigate effects of surface concave-convex and zig-zag micro-arrays on EMI shielding of multiwalled carbon nanotubes/polydimethylsiloxane composites (MWCNT/PDMS) in the C- and X-band, as PDMS can be easy to endow various functions by adding functional particles [65]. During the initial simulations, we aim to achieve strong electromagnetic shielding performance through straightforward structural designs. The energy of EMWs attenuates as their propagation path increases, with this path extension primarily resulting from the resonator effect and multiple reflections/scatterings [66]. The reflection/scattering of EMWs typically occur at the material's surface or at internal heterogeneous interfaces. The resonator effect can be created in surface concave-convex structure. Hence, we opt for simple cylindrical and rectangular concave-convex patterns. The design of the zig-zag structure is based on the layer-by-layer stacking principle of a 3D printer. A comparative study is mainly carried on three different surface structures, i.e. plane (P), surface stripe concave-convex (SSC), surface cylindrical concave-convex (SCC) structures, and these surface concave-convex structures with or without secondary zig-zag micro-arrays. The simulated EMI shielding performance in the C- and X-band is firstly obtained by electromagnetic simulation so as to select the optimal surface micro-arrays. For the sample preparation, a 3D printer is used to print acrylonitrile-butadiene-styrene copolymer (ABS) molds which are complementary with the designed surface concave-convex micro-arrays. Subsequently, the MWCNT/PDMS specimens with specific surface structures are fabricated via curing in the ABS molds. Both the simulation and experimental results show that the SSC and SCC samples with secondary zig-zag micro-arrays have higher EMI shielding performance than the P samples in both X and C bands. The EMI shielding mechanism is also discussed based on these specific surface structures. This study can provide a new idea for the development of efficient EMI shielding materials in low frequency via constructing a specific micro-arrays on the surface.

2 Experimental section

2.1 Materials

MWCNT (NC7000), was purchased from Nanocyl S.A Company in Belgium. PDMS (Sylgard 184), consists of a base elastomer and a corresponding curing agent, was bought from Dow Corning Company in the United States. ABS wire (diameter: 1.75 mm, printing temperature at 245–265 °C) was provided by INTAMSYS Company.

2.2 Sample preparation

Figure 1 illustrates preparation procedures for the samples with surface concave-convex and zig-zag micro-arrays. Firstly, the samples with micro-arrays are constructed in the electromagnetic simulation software ANSYS HFSS. After the simulation, the effective models are selected and then recognized by a 3D printer which is complementary to the micro-arrays. The model slicing analysis is carried out in INTAMSUITE 4.0 slicing software, and the sliced model information is transferred to the 3D printer (FUNMAT HT, Shanghai Yuanzhu Intelligent Technology Co., Ltd, China) to print ABS molds with specific surface structure. Secondly, PDMS is dissolved in n-hexane, and then MWCNTs are added. The MWCNTs are evenly dispersed in the PDMS solution by an ultrasonic treatment for 10 min. Subsequently, the

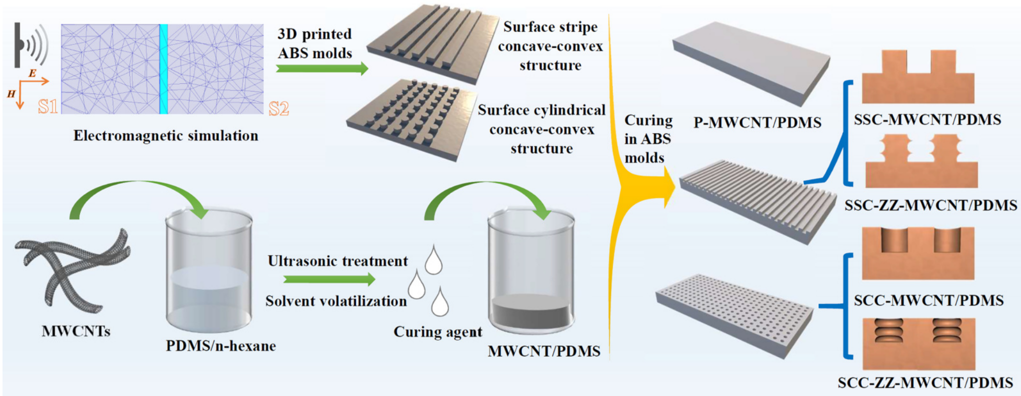

Figure 1 Schematic diagram for preparing samples containing a surface concave-convex structure with and without zig-zag micro-arrays.

MWCNT/PDMS/n-hexane solution is heated to a temperature of 70 °C and maintained for 12 h to completely volatilize n-hexane. After that, the curing agent with a mass ratio of 1/10 to PDMS is added, and the curing agent is mixed with MWCNT/PDMS by manual stirring. Thirdly, the MWCNT/PDMS mixed with the curing agent is filled into the ABS molds and cured at 100 °C for 2 h in vacuum. The different content of MWCNTs of 3 wt.%, 5 wt.%, and 7 wt.% are chosen in MWCNT/PDMS to study the effects of electrical conductivity on the EMI shielding properties of the samples with surface micro-arrays. For convenience, the samples are denoted as *X*-Y-ZZ-MWCNT/PDMS with both concave-convex and zig-zag micro-arrays, where *X* is the concentration of MWCNTs, and Y is the type of the surface concave-convex micro-arrays. For instance, the 3-SSC-ZZ-MWCNT/PDMS code means that the content of MWCNTs is 3 wt.% and the surface type is a surface stripe concave-convex and zig-zag micro-arrays. Samples with only concave-convex micro-arrays were prepared using metal molds for comparison, denoted as *X*-Y-MWCNT/PDMS.

2.3 Characterization

The electromagnetic interference shielding mechanism of the samples with three surface micro-arrays was simulated and analyzed by using an electromagnetic simulation. A polarizing microscope (PLM, Olympus BX51) was used to observe the size of the surface and concave-convex structure of the samples. A field emission scanning electron microscopy (FESEM, JSM-7800F) was carried to observe the distribution of MWCNTs and the morphology of samples. A four-probe tester (RTS-8, Guangzhou Four-Point Probe Technology Co., Ltd., China) was conducted to test the conductivity of the specimens with different MWCNTs concentrations. A vector network analyzer (3672E, Ceyear Technologies Co., Ltd, China) was used to test the electromagnetic parameters such as S_{11} and S_{21} of the samples in the X-band and C-band by a waveguide transmission line method. The absorption (A), reflection (R), and transmission (T) coefficients of the samples are calculated from the parameters S_{11} and S_{21} via Eqs. (1)–(3) [67–69].

$$R = |S_{11}|^2 \tag{1}$$

$$T = |S_{21}|^2 \tag{2}$$

$$A = 1 - R - T \tag{3}$$

3 Results and discussion

3.1 Electromagnetic simulation

The EMI shielding properties for the specimens with surface micro-arrays was firstly simulated at the C-band and X-band. The simulation software tool is ANSYS HFSS. Simulation of electromagnetic shielding performance was achieved by configuring a rectangular waveguide cavity to mimic real-world testing conditions. Simulation parameters are shown as follow: Modal. and the analog band is C-band (4.0–8.2 GHz), X-band (8.2–12.4 GHz). The corresponding to the model dimensions length, width, and height are 47.55 mm × 22.15 mm × 3.00 mm (corresponds to the 4–6 GHz band), 34.85 mm ×15.80 mm ×3.00 mm (corresponds to the 6–8.2 GHz band), and 22.86 mm × 10.16 mm × 3.00 mm (corresponds to the 8.2–12.4 GHz band). These models are placed in the center of the cavity. The custom material conductivity is used for all models. The boundary condition is Perfect E. The wave port excitation is set at both ends of the cavity. The port impedance is normalized to 50 Ω. Adaptive meshing is used in the solution settings with a convergence precision of 0.02 Δ*S*. The highest frequency of each band is used as the adaptive meshing processing frequency. Interpolating sweep is used for frequency scanning.

Table S1 and Fig. S1 in the Electronic Supplementary Material (ESM) gives the simulation results for the P, SSC, and SCC structure models with different size of the structure. The width and depth of the micro-arrays have more or less affect the EMI shielding performance of the samples. The small size of the micro-arrays have the better shielding performance on a whole. However, in this study, the depth of the concave-convex micro-arrays set at 0.70 mm, the stripe width and cylindrical radius is 0.70 mm, respectively, taking consideration of the print resolution of the 3D printer. The custom conductivity of the model material is 50, 150, and 500 S/m to study the effect of conductivity on EMI SE. The conductivity settings are based on the conductivity of the MWCNT/PDMS composites, with different conductivity parameters ranging from low to high. The conductivity setting of 150 S/m for the remaining simulations is chosen because the conductivity of MWCNT/PDMS composites with 7 wt.% MWCNTs is close to 150 S/m. The other parameters are kept at the default value. Through the port translation setting, the wave port excitation at both ends of the cavity is approximately on both sides of the model to eliminate the phase change of EMWs emitted from the two wave ports.

The distribution of electric field energy in each model under varying conductivity and across different wavelength bands is acquired by analyzing the field distribution from the simulation results. Figures 2(a)–2(e) illustrate the simulated electric field energy distribution for each model at a conductivity of 150 S/m. The shielding effect of the model on electromagnetic waves is evident when comparing the distribution of electric field energy without the sample (Fig. 2(a)) and with the planar sample (Fig. 2(b)). The samples in Fig. 2(b) are located within the yellow dashed boxes and the model is placed in the center of the waveguide cavity while parallel to the ports on both sides. Firstly, the rapid attenuation of internal electric field energy is found in the plane model across each frequency band, indicating that the shielding mechanism of the P sample is primarily due to the reflection loss induced by reflecting electromagnetic waves (Figs. 2(c1)–2(e1)). Secondly, the concentration of electric field energy in the samples with the concave-convex structure in the cross-sections shows that the shielding mechanism of the samples with SC structure against electromagnetic waves is primarily due to the multiple reflections of electromagnetic waves at the concave-convex micro-arrays. In comparison of the SCC samples, the SSC samples have weaker multiple reflections of SSC on electromagnetic waves resulting in a broader distribution of electric field energy across the cross-section of the model.

Thirdly, due to the enhanced penetration capability and decreased energy as the frequency of electromagnetic waves decreases, the cross-sectional distribution of electric field energy for the P, SSC, and SCC samples becomes widely with decreasing the frequency. Fourthly, the enhancement of impedance matching with low conductivity diminishes the microwave reflection on the surface of the samples, thereby increasing the absorption loss of electromagnetic waves, as shown in Fig. S2 in the ESM. Conversely, the high conductivity enhances the surface reflection and reduces absorption loss of electromagnetic waves, as shown in Fig. S3 in the ESM.

Figures 2(f)–2(h) show the simulation results of the samples with different concave-convex structure and different conductivity. Obviously, with the increase of conductivity, the specimens with SSC structure have better EMI shielding performance (S_{21}) than the P and SCC structures. For example, when the conductivity is 50 S/m, the SSC samples has worse shielding performance than the P samples at different frequencies. When the conductivity increases gradually, the S_{21} value of the SSC samples in the C-band is higher than that of the P samples and increases with the increase of conductivity. Specifically, in the 6.0–8.2 GHz band, when the conductivity is 500 S/m, the S_{21} value of the SSC samples is 8.0 dB higher than the P samples. Comparing with the planar structure, the SCC samples show a trend of better shielding performance with the decrease of frequency, and this trend can be enhanced with the increase of conductivity. The shielding performance of SCC is

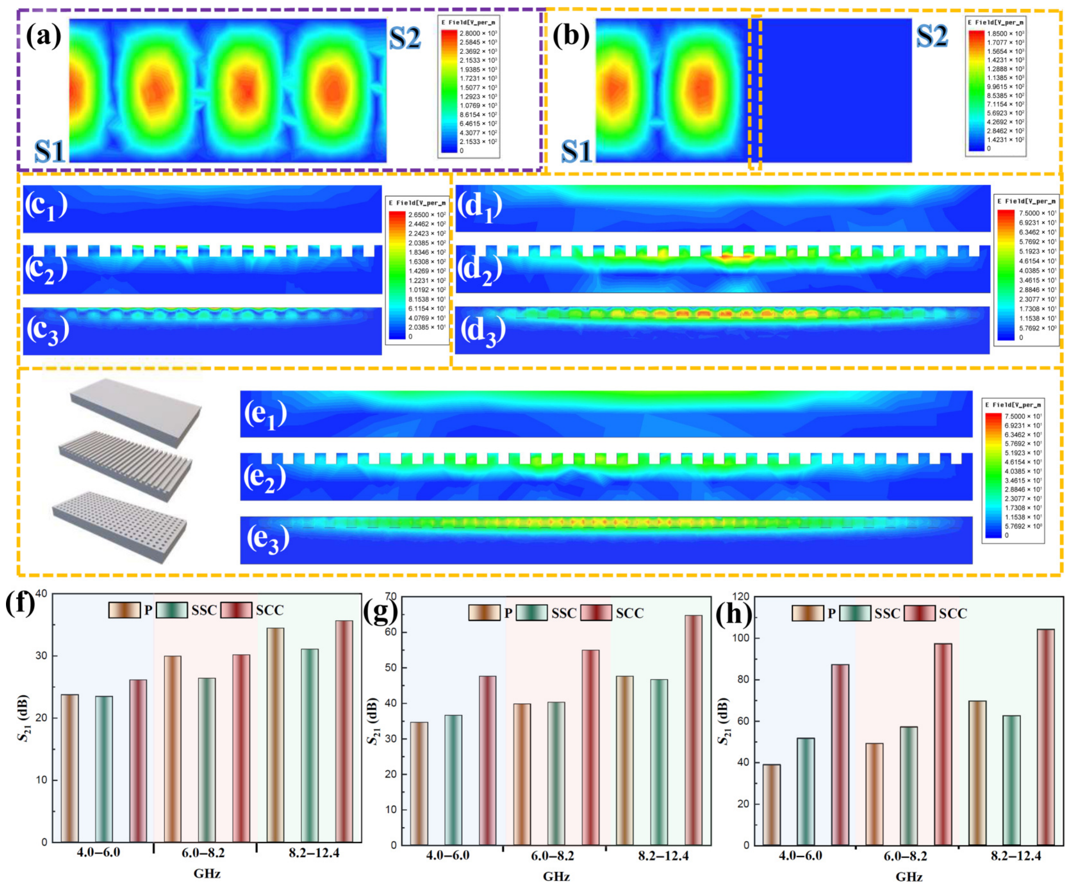

Figure 2 The distribution of electric field energy in the cavity (a) without and (b) with a planar sample are located within the yellow dashed boxes. Electric field energy distribution of different structural model of (c1)–(e1) the P samples, (c2)–(e2) the SSC samples, and (c3)–(e3) the SCC samples cross-sections with the conductivity of 150 S/m in the frequency range of (c1)–(c3) 8.2–12.4 GHz, (d1)–(d3) 6.0–8.2 GHz, and (e1)–(e3) 4.0–6.0 GHz, respectively. Simulation results of electromagnetic interference shielding performance (S21) for the samples with P, SSC, and SCC surface micro-arrays with different conductivities of (f) 50, (g) 150, and (h) 500 S/m, respectively.

stronger than that of planar structure and SSC under different conductivity and different wavelength bands. Furthermore, the conductivity has a greater influence on the EMI shielding performance of the SCC samples.

Furthermore, the EMI shielding performance of the three models on EMWs decreases with the decrease of frequency. The EMI shielding performance of the SCC-MWCNT/PDMS specimens under different frequency ranges is higher than that of the other two specimens at the C- and X-band. Specifically, the S_{21} value of the SCC-MWCNT/PDMS samples with set conductivity of 500 S/m is ~ 87 dB, which is 67% and 123% higher than ~ 52 and ~ 39 dB of the SSC-MWCNT/PDMS and P-MWCNT/PDMS samples at the frequency range of 4.0–6.0 GHz, respectively. For the SSC-MWCNT/PDMS specimens, the S_{21} values at high conductivity (500 S/m) are higher than the corresponding values of the P-MWCNT/PDMS specimens at the C-band, while the S_{21} values are close to the corresponding values of the P-MWCNT/PDMS specimens with low conductivity (50 and 150 S/m) at the C- and X-band. With the decrease of frequency, the S_{21} value of the SSC samples is lower than that of the P samples with the same conductivity in the X-band, but the S_{21} value of the SSC samples is close to or even higher than that of the P samples in the 4.0–6.0 GHz band. Specifically, the S_{21} value of the SSC samples is ~ 7 dB lower than that of the P samples at the conductivity of 500 S/m at X-band, while the S_{21} value of the SSC samples is ~ 13 dB higher than that of the P samples in the range of 4.0–6.0 GHz, as shown in Fig. 2(h).

Figure 3 compares the cross-sectional distribution of electric field energy for the SC models with or without a secondary zig-zag micro-arrays at a conductivity of 150 S/m and an electromagnetic wave frequency of 8.2–12.4 GHz. The construction of this secondary zig-zag micro-arrays can further concentrate the electric field energy within the SC structure. Following the construction of secondary zig-zag micro-arrays, the distribution of electric field energy in SSC transforms from being deep within the model to becoming concentrated at the SSC structure. For the electric field energy distribution in SCC structure, a shift from concentration at the convex part of the SCC structure is found to concentrate at the interface of the secondary zig-zag micro-arrays. The alteration is more pronounced in the electric field energy distribution of SCC-

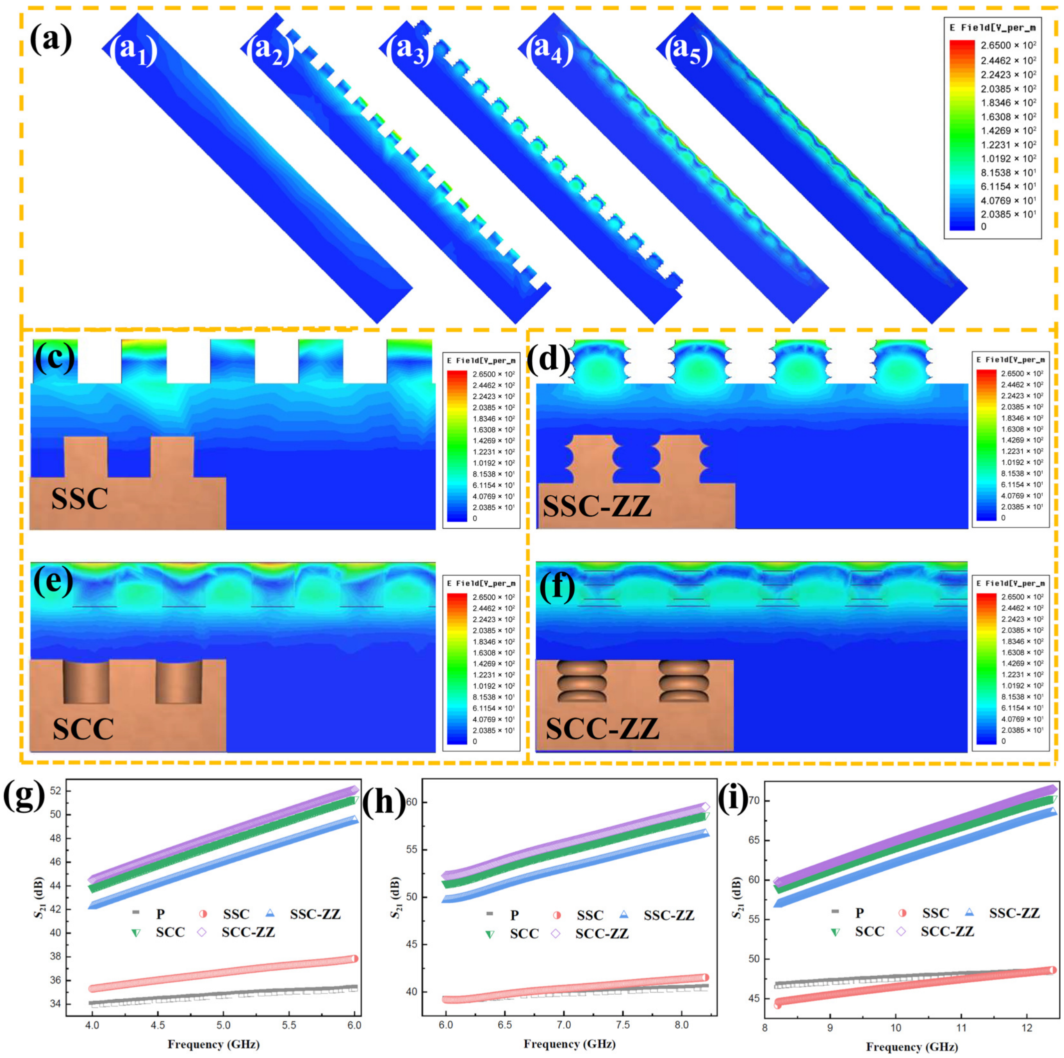

Figure 3 Cross-sectional electric field energy distributions of (a1) P, (a2) SSC, (a3) SSC-ZZ, (a4) SSC, and (a5) SCC-ZZ at the frequency range of 8.2–12.4 GHz. Detailed comparison of electric field energy distributions for (c) SSC, (d) SSC-ZZ, (e) SCC, and (f) SCC-ZZ. Comparison of the electromagnetic interference shielding performance of the model with or without zig-zag micro-arrays and the flat model with the conductivity of 150 S/m at each wavelength band of (g) 4.0–6.0, (h) 6.0–8.2, (i) 8.2–12.4 GHz, respectively.

ZZ at lower wavelengths, such as 6.0–8.2 GHz (Fig. S4 in the ESM) and 4.0–6.0 GHz (Fig. S5 in the ESM). The shift in electric field energy distribution following the construction of the secondary zig-zag micro-arrays in both SSC and SCC samples demonstrates that electromagnetic wave energy becomes concentrated in the SC structure due to multiple scattering and interference cancellation at the secondary zig-zag micro-arrays.

Figures 3(g)–3(i) give the simulated S_{21} values of the samples with SC structure and with or without zig-zag micro-arrays at a conductivity of 150 S/m. The shielding performance of the two SC structure models, especially the SSC samples, is obviously improved when the secondary zig-zag micro-arrays is constructed. Specifically, the mean S_{21} value of the SCC samples without secondary zig-zag micro-arrays is close to the P samples, while the SCC-ZZ samples have ~ 15 dB higher S_{21} value than the P samples at X-band.

3.2 Morphology of the samples with surface micro-arrays

Figures 4(a)–4(c) depict digital optical images for the 5-P-ZZ-MWCNT/PDMS, 5-SSC-ZZ-MWCNT/PDMS, and 5-SCC-ZZ-MWCNT/PDMS samples, respectively. It can be observed that the regular SC structure has been successfully constructed. The depth and width of the SC structure is in the range between 0.7 to 0.8 mm, as shown in Fig. S6 in the ESM. The different size of samples with surface micro-arrays is fabricated for the test requirement, as shown in Fig. S7 in the ESM. The surface morphology of the P sample can be found without any micro-arrays (Fig. 4(d)).

For the samples with SC structure, the vertical view and cross sections of the samples are observed to give the accurate characterization for the structure of the samples. Figures 4(e1) and 4(e2) give the vertical view of the 5-SSC-MWCNT/PDMS and 5-SSC-ZZ-MWCNT/PDMS samples, while Figs. 4(f1) and 4(f2) show the vertical view of the 5-SCC-MWCNT/PDMS and 5-SCC-ZZ-MWCNT/PDMS samples. Clearly, the samples without zig-zag micro-arrays have smooth surfaces at the SC structure while the samples with zig-zag micro-arrays exhibit rough surfaces at the SC structure. The cross-sections of the SC structure samples clearly indicate the zig-zag micro-arrays. Figures 4(g) and 4(j) depict the cross-sections of the 5-SSC-MWCNTs/PDMS and 5-SCC-MWCNTs/PDMS samples without zig-zag micro-arrays. The above two samples have regular SC structure with smooth surfaces. However, the zig-zag micro-arrays are found in the 5-SSC-ZZ-MWCNTs/PDMS and 5-SCC-ZZ-MWCNTs/PDMS samples, as

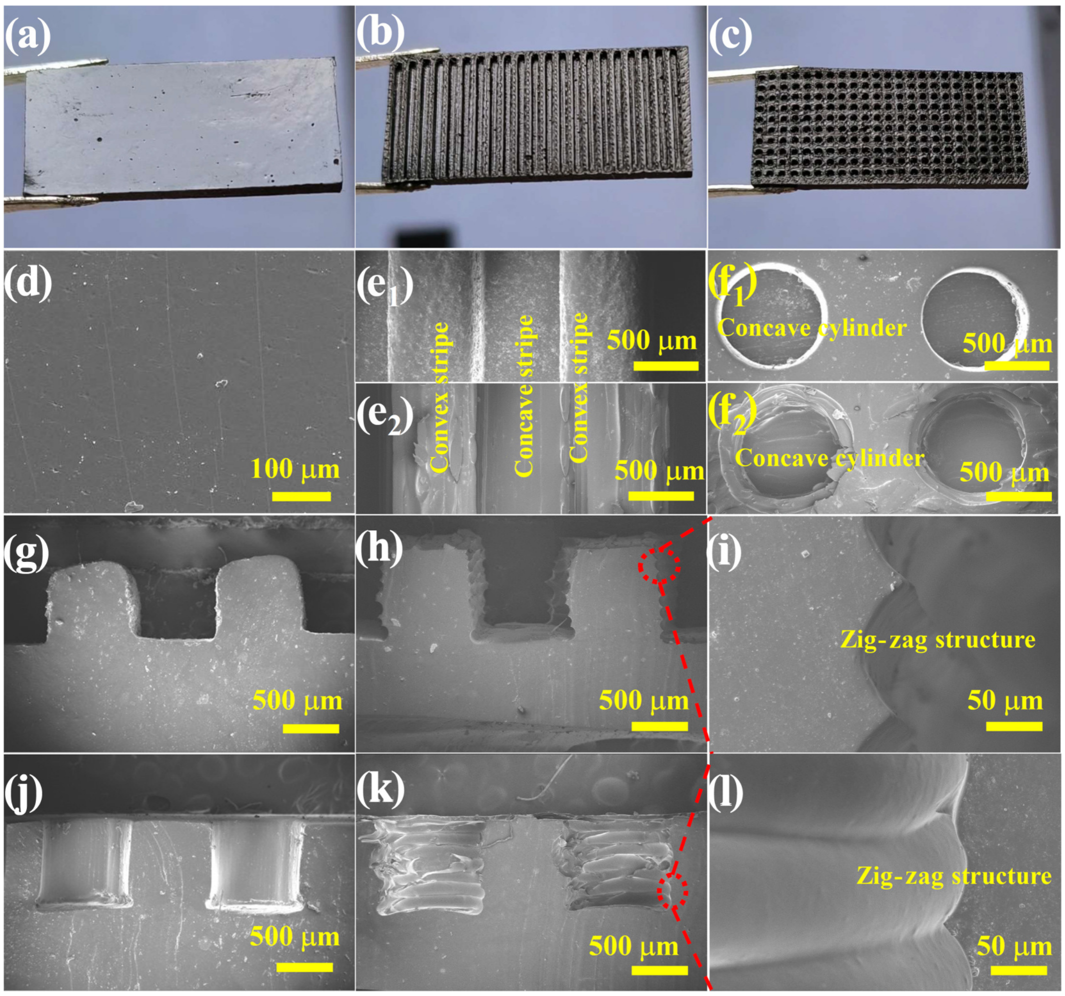

Figure 4 Digital optical images of (a) 5-P-MWCNT/PDMS, (b) 5-SSC-ZZ-MWCNT/PDMS, and (c) 5-SCC-ZZ-MWCNT/PDMS samples. FESEM images of the surface morphology of (d) 5-P-CP, (e1) 5-SSC-MWCNT/PDMS, (e2) 5-SSC-ZZ-MWCNT/PDMS, (f1) 5-SCC-MWCNT/PDMS, and (f2) 5-SCC-ZZ-MWCNT/PDMS samples. FESEM images of cross-sections for (g) 5-SSC-MWCNT/PDMS, (h) and (i) 5-SSC-ZZ-MWCNT/PDMS, (j) 5-SCC-MWCNT/PDMS, and (k) and (l) 5-SCC-ZZ-MWCNT/PDMS samples.

shown in Figs. 4(h), 4(i), 4(k) and 4(l). In addition, the cross-sections of samples containing different amount MWCNTs are also evaluated at concentrations of 3 wt.%, 5 wt.%, and 7 wt.% are illustrated in Figs. S2(a)–S2(c) in the ESM. The distribution of MWCNTs within the PDMS matrix is uniform and progressively become dense with increasing the content of MWCNTs. Certainly, the electrical conductivity is enhanced by adding more MWCNTs, as shown in Fig. S8 in the ESM.

3.3 Electromagnetic interference shielding performance

Figures 5(a)–5(c) depict the EMI shielding performance of the P, SSC, SSC-ZZ, SCC, and SCC-ZZ samples with different content of MWCNTs. Obviously, the SC samples with zig-zag micro-arrays have higher EMI SE values than the P samples and the SC samples without zig-zag micro-arrays. Specifically, the EMI SE of the 3-SSC-ZZ-MWCNT/PDMS and 3-SCC-ZZ-MWCNT/PDMS samples are ~ 34.0 dB, while the EMI SE of the 3-SSC-MWCNT/PDMS and 3-SCC-MWCNT/PDMS samples are ~ 28.2 and ~ 30.3 dB at X-band, respectively (Fig. 5(a)). When the content of MWCNTs increases to 7 wt.%, the SSC and SCC samples demonstrate an escalation from approximately ~ 44.6 and ~ 49.9 dB to roughly ~ 54.3 and ~ 56.4 dB after the implementation of the secondary zig-zag micro-arrays (Fig. 5(c)). The maximum increment can approach ~ 10 dB. As shown in Fig. 5(c), the instability of the SE at higher frequency ranges is attributed to the increase in electromagnetic wave shielding performance of the composites with frequency. However, the high EMI SE values usually result in a serious baseline fluctuation. In this study, the rectangular waveguide test method we employed tends to become gradually unstable when the EMI SE approaches and exceeds 50 dB.

Furthermore, the SSC and SCC samples have lower EMI shielding performance than that of the P samples. The EMI SE reduction of the SSC and SCC samples may be attributed to the decrease of the sample quality when introducing the surface micro-arrays on the surface. At the same thickness, the construction of a surface micro-arrays definitely reduce the quality of materials, as shown in Table S2 in the ESM. Simultaneously, the low EMI SE of the SSC and SCC samples demonstrates that the incorporation of secondary zig-zag micro-arrays can notably enhance the microwave shielding performance, which is consistent with the simulation results. The performance of the SCC and SSC structures in Figs. 5(a)–5(c) is poorer compared to the P structure, which differs from the simulation results in Fig. 3. This is attributed to the non-uniform conductivity and structure of the fabricated samples, which can influence the electromagnetic shielding performance. Such issues are not present in the complex serrated structure samples because the serrated structure exhibits stronger absorption of electromagnetic waves, mitigating these effects.

Figures 5(d)–5(f) depict the EMI shielding performance of the P-MWCNT/PDMS, SSC-ZZ-MWCNT/PDMS, and SCC-ZZ-

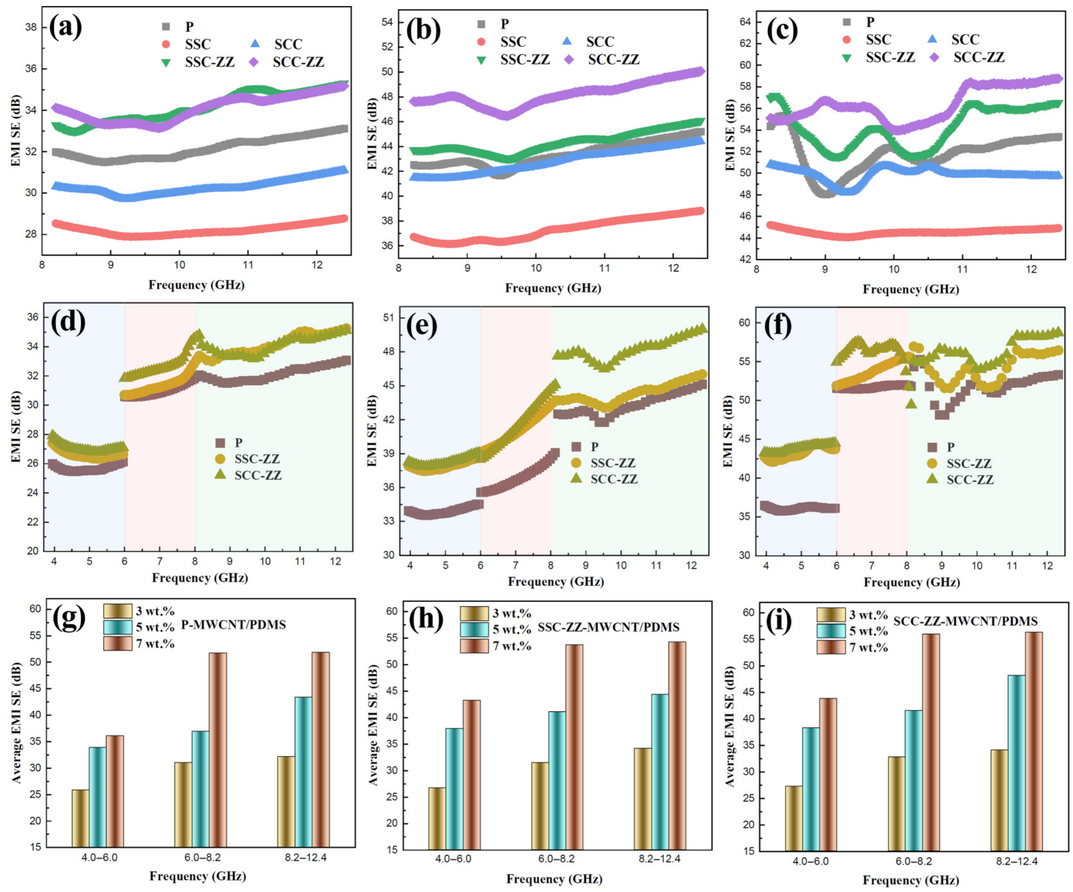

Figure 5 EMI SE versus frequency for the P-MWCNT/PDMS, SSC-MWCNT/PDMS, SSC-ZZ-MWCNT/PDMS, SCC-MWCNT/PDMS and SCC-ZZ-MWCNT/PDMS samples containing different MWCNTs loadings of (a) 3 wt.%, (b) 5 wt.%, and (c) 7 wt.% at X-band. EMI SE versus frequency for the P-MWCNT/PDMS, SSC-ZZ-MWCNT/PDMS, and SCC-ZZ-MWCNT/PDMS samples containing different MWCNTs loadings of (d) 3 wt.%, (e) 5 wt.%, and (f) 7 wt.% at C- and X-band. Average EMI SE values of the (g) P-MWCNT/PDMS, (h) SSC-ZZ-MWCNT/PDMS, and (i) SCC-ZZ-MWCNT/PDMS samples containing different MWCNTs loadings and at different frequency range.

MWCNT/PDMS samples containing different MWCNTs loadings at C- and X-band. First of all, the EMI SE of the three structural samples increases with the increase of MWCNT loadings. Second, the SCC-ZZ-MWCNT/PDMS specimens exhibit the highest EMI SE values when containing the same content of MWCNT and in the same frequency range, which is consistent with the simulation results (Fig. S8 in the ESM). Specifically, the EMI shielding performance of 7-SCC-ZZ-MWCNT/PDMS can reach a maximum value of approximately 58.8 dB, indicating that the augmentation of EMI shielding properties in composite materials can be achieved through the construction of a concave-convex and zig-zag micro-arrays. Although the differences among the samples are minimal, all samples exhibit a consistent trend. It should point out that the variation of EMI SE values in different ranges of 4–6, 6–8.2 and 8.2–12.4 GHz is discontinuous. There are two different EMI SE values at 6 and 8 GHz. This discontinuity arises because the rectangular waveguide testing method utilizes fixtures and samples with different sizes. The different frequency band has different calibration modes which leads to the observed discontinuity in the EMI SE values. In addition, two different calibration modes and fixtures are used at 6 and 8 GHz which leads to two different values at 6 and 8 GHz.

Moreover, the distribution of MWCNT shown in Fig. S9 in the ESM appears homogeneous, indicating that this discrepancy comes from the construction of the micro-arrays structure but not attributable to the MWCNT distribution of the material. As can be observed in Figs. 5(d)–5(f), the reason for the lack of continuity in the SE data at these frequencies is that the different rectangular waveguide fixtures vary with the test band. Third, the microwave shielding enhancement on electromagnetic waves of the SCC structure is superior to that of the SSC structure. Notably, at the frequency range of 4.0–12.8 GHz, the EMI SE of the 3-SSC-ZZ-MWCNT/PDMS and 3-SCC-ZZ-MWCNT/PDMS samples are higher than that of 3-P-MWCNTs/PDMS samples. With an increase in MWCNTs content to 7 wt.%, the EMI SE of 7-SCC-ZZ-MWCNT/PDMS in the 4.0–6.0 GHz band demonstrates an enhancement of approximately 7.7 dB in comparison of the 7-P-MWCNTs/PDMS samples, as shown in Figs. 5(g)–5(i). In addition, the EMI SE values of the three structural samples diminish as the electromagnetic wave frequency decreases at the same content of MWCNTs. The results indicate that the shielding enhancement effect of the surface micro-arrays is less influenced by changing electromagnetic wave frequency.

3.4 Electromagnetic shielding mechanism

The above results indicate that the SC structure and the secondary zig-zag micro-arrays significantly impact the shielding performance of the samples. The absorption coefficient (*A*) and reflection coefficient (*R*) are calculate for both the SC samples and the planar samples to analyze the impact of the SC structure and the secondary zig-zag micro-arrays on shielding mechanism. The transmission coefficient (*T*) is very small for all the samples (Fig. S10 in the ESM and Fig. 6(c)), suggesting the excellent microwave shielding performance. First, the *A* value of the SSC and SCC samples is higher than the P samples with three different MWCNT contents, as shown in Fig. 6(a). The results may be ascribed to the

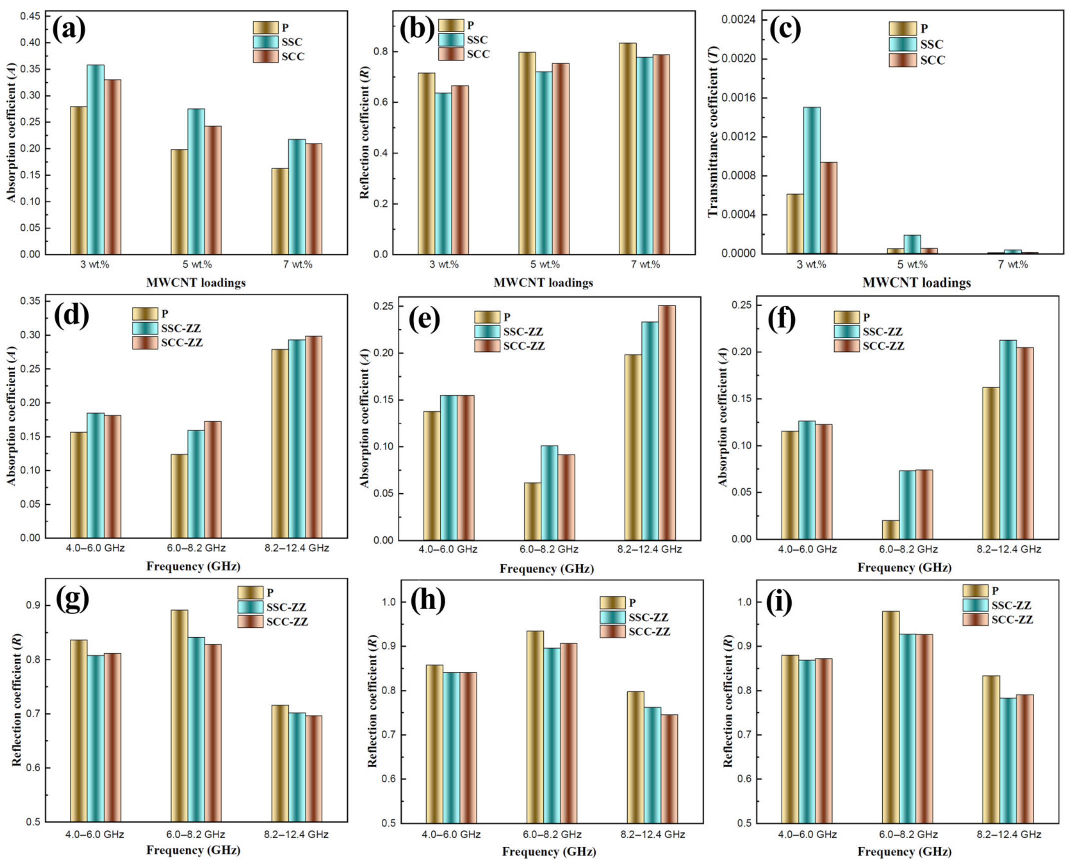

Figure 6 (a) Absorption coefficient (*A*), (b) reflection coefficient (*R*), and (c) transmission coefficient (*T*) of the P, SSC and SCC samples with different MWCNT loadings at X-band. flat SC sample. (d)–(f) The *A* and (g)–(i) *R* of the samples with different MWCNT content of ((d) and (g)) 3 wt.%, ((e) and (h)) 5 wt.%, and ((f) and (i)) 7 wt.% at C- and X-band, respectively.

enhancement of multiple reflection/scattering within the surface micro-arrays. The electromagnetic waves are attenuated due to the increased propagation path resulting from multiple reflections and scattering. With each reflection and scattering, the energy diminishes, leading to an elevation in the *A* values. However, the flat surface of the P samples fails to induce multiple reflection/scattering of electromagnetic waves.

Second, all the P, SSC and SCC samples show the lower *A* values than the *R* values (Fig. 6(b)), suggesting the microwave shieling mechanism is mainly reflection mode. Third, the *A* value of the SC sample with the secondary zig-zag micro-arrays remains higher than that of the P samples with the same MWCNT loadings and the same frequency range (Figs. 6(d)–6(f)). The results indicate that the construction of the secondary zig-zag micro-arrays improves the attenuation of electromagnetic waves within the SC structure, thereby increasing the absorption loss of the sample. The absorption loss of electromagnetic waves by the secondary zig-zag micro-arrays may result from multiple reflections of electromagnetic waves at the SC structure and multiple scattering at the secondary micro-arrays. Forth, the increase in material conductivity enhances the reflection capability of the material towards electromagnetic waves, because the *A* values of the sample decrease with increasing MWCNT contents, as depicted in Figs. 6(d)–6(f). Finally, the *R* values in three frequency range are higher than the *A* values and increase with the elevation of MWCNT contents as shown in Figs. 6(g)–6(i). Higher conductivity leads to a more robust electromagnetic wave reflection of the sample, enhancing surface reflections.

Figure S11 in the ESM shows comparison of the *A*, *R* and *T* values for the samples with and without secondary zig-zag micro-arrays. Samples with secondary zig-zag micro-arrays exhibit a slight reduction in absorption coefficient due to enhanced reflection and scattering of electromagnetic waves at the secondary zig-zag micro-arrays. Particularly for the SCC samples, the addition of serrations results in a larger decrease in absorption coefficient (*A*). As the conductivity increases, the *A* values of SSC-ZZ and SCC-ZZ gradually approach those of SSC and SCC, respectively. Nevertheless, the secondary zig-zag micro-arrays can obviously enhance electromagnetic wave shielding with increasing conductivity. In addition, Fig. S12 in the ESM show the simulation results for the samples with larger and smaller zig-zag micro-arrays. The results show that variations in the size of the zig-zag micro-arrays lead to only slight changes in the EMI shielding performance of the samples. Additionally, the attenuation image of electromagnetic waves by the three different sizes of zig-zag micro-arrays is found to be essentially the same.

In summary, the combined analysis of *A* and *R* values of the sample along with simulated energy distribution for electric field reveals that the microeave shielding mechanism is primarily related with the surface concave-convex and zig-zag micro-arrays for the samples, as illustrated in Fig. 7. Multiple reflections of electromagnetic waves may occur at the concave-convex structure (Fig. 7(a)), and multiple scattering of electromagnetic waves takes place in the secondary zig-zag micro-arrays of the concave-convex structure (Fig. 7(b)). Furthermore, the surface concave-convex can create resonator effect to attenuate microwaves. In addition, the interference cancellation occurs after electromagnetic waves undergo multiple reflections and scatterings at the concave-convex structure (Fig. 7(c)). Certainly, conduction losses between MWCNT-MWCNT interface and interfacial polarization losses between MWCNT-PDMS are also contributed to the excellent microwave shielding performance (Fig. 7(d)).

4 Conclusions

In this study, the electromagnetic simulation was firstly carried to predict the surface micro-arrays of the MWCNT/PDMS composites with highly efficient microwave shielding at the C- and X-bands. According to the simulation, the microwave shielding MWCNT/PDMS composites with surface concave-convex and zig-zag micro-arrays were prepared via a compression molding in special molds, which were designed by a 3D printer. Expectedly, the

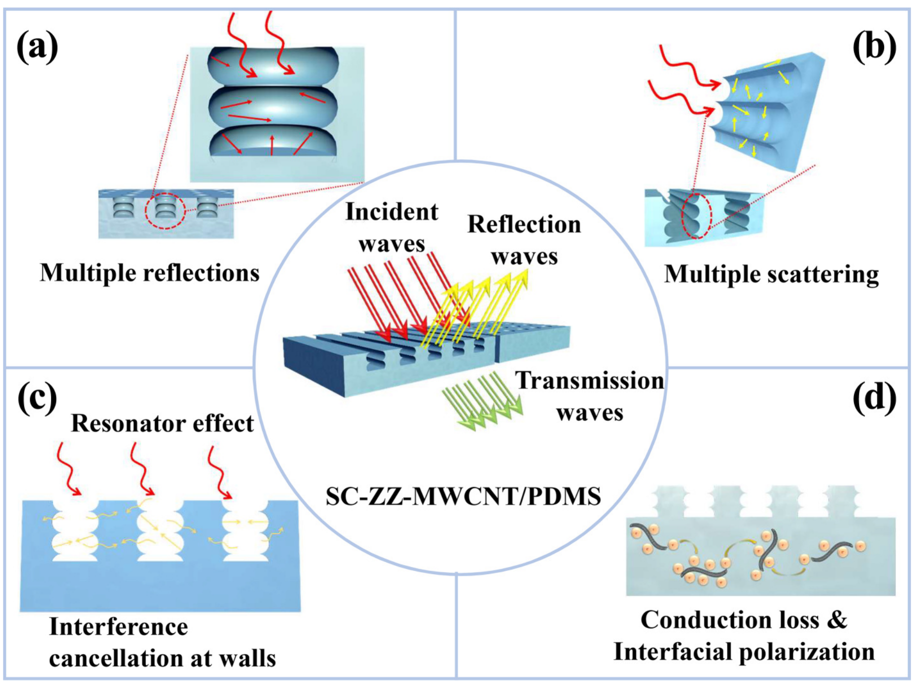

Figure 7 Schematic draw for EMI shielding mechanism of the samples with surface concave-convex and zig-zag micro-arrays.

experimental results is consistent with simulation results for the samples at the C- and X-bands. The introduction of secondary zig-zag micro-arrays can allow SC-MWCNT/PDMS to augment the electromagnetic interference shielding effectiveness obviously. For instance, the EMI SE values of 7-SSC-ZZ-MWCNT/PDMS are ~ 7.7 and ~ 9.7 dB higher than the value of 7-SSC-MWCNT/PDMS in the frequency range of 4.0–6.0 and 8.2–12.4 GHz, respectively. The microwave shielding enhancement mechanism in the SC-ZZ-MWCNT/PDMS samples primarily arises from resonator effect, multiple reflections, multiple scattering, and interference cancellation of electromagnetic waves at the concave-convex and zig-zag micro-arrays, thereby enhancing the absorption loss and EMI shielding properties of the materials.

Electronic Supplementary Material: Supplementary material (simulation results , electric field energy distribution maps, and optical micrographs of the samples, average EMI SE values of each surface structure samples with different conductivity, distribution of MWCNTs in the samples, transmission coefficients (*T*) of the samples) is available in the online version of this article at https://doi.org/10.26599/NR.2025.94907153.

Data availability

All data needed to support the conclusions in the paper are presented in the manuscript and the Electronic Supplementary Material. Additional data related to this paper may be requested from the corresponding author upon request.

Acknowledgements

We thank National Natural Science Foundation of China (No. 52173264), Natural Science Foundation Project of Chongqing (No. cstc2024ycjh-bgzxm0005) and Fundamental Research Funds for the Central Universities (No. SWU-XDJH202314) for financial support. The authors thanks Dr. Xi Tang in Southwest University for the technical support in the use of the vector network analyzer.

Declaration of competing interest

All the contributing authors report no conflict of interests in this work.

Author contribution statement

K. J.: Data curation, validation, writing manuscript, experimental design. Z.-C. J.: Data curation, validation, experimental design. Y. C. Z.: Data curation, experimental design, writing manuscript. S. H.: Supervision, methodology. M. W.: Writing – review & editing, supervision, methodology, conceptualization. All the authors have approved the final manuscript.

Use of AI statement

None.

References

[1] He, M. K.; Zhong, X.; Lu, X. H.; Hu, J. W.; Ruan, K. P.; Guo, H.; Zhang, Y. L.; Guo, Y. Q.; Gu, J. W. Excellent low-frequency microwave absorption and high thermal conductivity in polydimethylsiloxane composites endowed by hydrangea-like CoNi@BN heterostructure fillers. *Adv. Mater.*, in press, DOI: 10.1002/adma.202410186.

[2] Isari, A. A.; Ghaffarkhah, A.; Hashemi, S. A.; Wuttke, S.; Arjmand, M. Structural design for EMI shielding: From underlying mechanisms to common pitfalls. *Adv. Mater.* **2024**, *36*, 2310683.

[3] Yang, Y.; Tao, J. R.; Yang, D.; He, Q. M.; Chen, X. D.; Wang, M. Improving dispersion and delamination of graphite in biodegradable starch materials via constructing cation-π interaction: Towards microwave shielding enhancement. *J. Mater. Sci. Technol.* **2022**, *129*, 196–205.

[4] He, M. K.; Hu, J. W.; Yan, H.; Zhong, X.; Zhang, Y. L.; Liu, P. B.; Kong, J.; Gu, J. W. Shape anisotropic chain-like CoNi/polydimethylsiloxane composite films with excellent low-frequency microwave absorption and high thermal conductivity. *Adv. Funct. Mater.*, in press, DOI: 10.1002/adfm.202316691.

[5] Tao, J. R.; Tang, X. H.; He, Q. M.; Wang, M. Effect of surface conductivity on electromagnetic shielding of multi-walled carbon nanotubes/poly(ε-caprolactone) composites. *Compos. Sci. Technol.* **2022**, *229*, 109715.

[6] Huang, M. L.; Luo, C. L.; Sun, C.; Zhao, K. Y.; Weng, Y. X.; Wang, M. Achieving absorption-type microwave shielding performance in polydimethylsiloxane/carbon nanotube sandwiched composites via regulating microwave interference effect. *Compos. Part A: Appl. Sci. Manuf.* **2023**, *169*, 107532.

[7] Yang, Y.; Luo, C. L.; Chen, X. D.; Wang, M. Sustainable electromagnetic shielding graphene/nanocellulose thin films with excellent joule heating and mechanical properties via *in-situ* mechanical exfoliation and crosslinking with cations. *Compos. Sci. Technol.* **2023**, *223*, 109913.

[8] Pan, F.; Shi, Y. Y.; Yang, Y.; Guo, H. T.; Li, L. X.; Jiang, H. J.; Wang, X.; Zeng, Z. H.; Lu, W. Porifera-inspired lightweight, thin, wrinkle-resistance, and multifunctional MXene foam. *Adv. Mater.* **2024**, *36*, 2311135.

[9] Yang, D.; Tao, J. R.; Yang, Y.; He, Q. M.; Wang, M. Robust microwave absorption in silver-cobalt hollow microspheres with heterointerfaces and electric–magnetic synergism: Towards achieving lightweight and absorption-type microwave shielding composites. *J. Mater. Sci. Technol.* **2023**, *138*, 245–255.

[10] Xu, J.; Fang, J. Y.; Zuo, P. Y.; Wang, Y. Z.; Zhuang, Q. X. Competitively assembled aramid-MXene Janus aerogel film exhibiting concurrently robust shielding and effective anti-reflection performance. *Adv. Funct. Mater.* **2024**, *34*, 2400732.

[11] Tao, J. R.; Luo, C. L.; Huang, M. L.; Weng, Y. X.; Wang, M. Construction of unique conductive networks in carbon nanotubes/polymer composites via poly(ε-caprolactone) inducing partial aggregation of carbon nanotubes for microwave shielding enhancement. *Compos. Part A: Appl. Sci. Manuf.* **2023**, *164*, 107304.

[12] Sambyal, P.; Noh, S. J.; Hong, J. P.; Kim, W. N.; Iqbal, A.; Hwang, S. S.; Hong, S. M.; Koo, C. M. FeSiAl/metal core shell hybrid composite with high-performance electromagnetic interference shielding. *Compos. Sci. Technol.* **2019**, *172*, 66–73.

[13] He, Q. M.; Tao, J. R.; Yang, D.; Yang, Y.; Wang, M. Surface wrinkles enhancing electromagnetic interference shielding of copper coated polydimethylsiloxane: A simulation and experimental study. *Chem. Eng. J.* **2023**, *454*, 140162.

[14] Chen, Z. B.; Yang, S. D.; Huang, J. H.; Gu, Y. F.; Huang, W. B.; Liu, S. Y.; Lin, Z. Q.; Zeng, Z. P.; Hu, Y. G.; Chen, Z. M. et al. Flexible, transparent and conductive metal mesh films with ultra-high FoM for stretchable heating and electromagnetic interference shielding. *Nano-Micro Lett.* **2024**, *16*, 92.

[15] Ruan, K. P.; Shi, X. T.; Zhang, Y. L.; Guo, Y. Q.; Zhong, X.; Gu, J. W. Electric-field-induced alignment of functionalized carbon nanotubes inside thermally conductive liquid crystalline polyimide composite films. *Angew. Chem., Int. Ed.* **2023**, *62*, e202309010.

[16] Bian, F. P.; Huang, R.; Li, X. B.; Hu, J. W.; Lin, S. D. Facile

construction of chestnut-like structural fireproof PDMS/Mxene@BN for advanced thermal management and electromagnetic shielding applications. *Adv. Sci.* **2024**, *11*, 2307482.
[17] Yang, J. M.; Wang, H.; Zhang, Y. L.; Zhang, H. X.; Gu, J. W. Layered structural PBAT composite foams for efficient electromagnetic interference shielding. *Nano-Micro Lett.* **2024**, *16*, 31.
[18] Yin, G.; Wu, J.; Ye, L.; Liu, L. X.; Yu, Y. X.; Min, P.; Yu, Z. Z.; Zhang, H. B. Dynamic adaptive wrinkle-structured silk fibroin/MXene composite fibers for switchable electromagnetic interference shielding. *Adv. Funct. Mater.*, in press, DOI: 10.1002/adfm.202314425.
[19] Fei, Y.; Liang, M.; Zhou, T.; Chen, Y.; Zou, H. W. Unique carbon nanofiber@ Co/C aerogel derived bacterial cellulose embedded zeolitic imidazolate frameworks for high-performance electromagnetic interference shielding. *Carbon.* **2020**, *167*, 575–584.
[20] Tolvanen, J.; Hannu, J.; Hietala, M.; Kordas, K.; Jantunen, H. Biodegradable multiphase poly(lactic acid)/biochar/graphite composites for electromagnetic interference shielding. *Compos. Sci. Technol.* **2019**, *181*, 107704.
[21] Ji, H.; Zhao, R.; Zhang, N.; Jin, C. X.; Lu, X. F.; Wang, C. Lightweight and flexible electrospun polymer nanofiber/metal nanoparticle hybrid membrane for high-performance electromagnetic interference shielding. *NPG Asia Mater.* **2018**, *10*, 749–760.
[22] Wang, Z.; Kong, Q. Q.; Yi, Z. L.; Xie, L. J.; Jia, H.; Chen, J. P.; Liu, D.; Jiang, D.; Chen, C. M. Electromagnetic interference shielding material for super-broadband: Multi-walled carbon nanotube/silver nanowire film with an ultrathin sandwich structure. *J. Mater. Chem. A* **2021**, *9*, 25999–26009.
[23] Zhao, W. W.; Xu, H. T.; Zhao, J. D.; Zhu, X. J.; Lu, Y. Y.; Ding, C. B.; He, W. J.; Bian, J.; Liu, L. L.; Ma, L. F. et al. Flexible, lightweight and multi-level superimposed titanium carbide films for enhanced electromagnetic interference shielding. *Chem. Eng. J.* **2022**, *437*, 135266.
[24] Sharma, A.; Babu, M. S.; Kumar, A. V.; Sarathi, R.; Subramanian, V. Electromagnetic shielding efficiency of carbon fibre fabric-sandwiched epoxy-MWCNT nanocomposites. *Bull. Mater. Sci.* **2022**, *45*, 44.
[25] Lee, J. H.; Jang, J. W.; Sohn, S. H.; Lee, S. G.; Park, M. S. Electromagnetic interference (EMI) shielding efficiency (SE) characteristics of the ITO/Ag multilayer structure. *Mol. Cryst. Liquid Cryst.* **2007**, *470*, 107–120.
[26] Li, M. Z.; Jia, L. C.; Zhang, X. P.; Yan, D. X.; Zhang, Q. C.; Li, Z. M. Robust carbon nanotube foam for efficient electromagnetic interference shielding and microwave absorption. *J. Colloid Interface Sci.* **2018**, *530*, 113–119.
[27] Zhang, H. M.; Zhang, G. C.; Li, J. T.; Fan, X.; Jing, Z. X.; Li, J. W.; Shi, X. T. Lightweight, multifunctional microcellular PMMA/Fe_3O_4@MWCNTs nanocomposite foams with efficient electromagnetic interference shielding. *Compos. Part A: Appl. Sci. Manuf.* **2017**, *100*, 128–138.
[28] Zhang, L. Y.; Liu, M.; Roy, S.; Chu, E. K.; See, K. Y.; Hu, X. Phthalonitrile-based carbon foam with high specific mechanical strength and superior electromagnetic interference shielding performance. *ACS Appl. Mater. Interfaces.* **2016**, *8*, 7422–7430.
[29] Fan, D. L.; Li, N. X.; Li, M. G.; Wang, S.; Li, S. X.; Tang, T. Polyurethane/polydopamine/graphene auxetic composite foam with high-efficient and tunable electromagnetic interference shielding performance. *Chem. Eng. J.* **2022**, *427*, 131635.
[30] Wang, T.; Kong, W. W.; Yu, W. C.; Gao, J. F.; Dai, K.; Yan, D. X.; Li, Z. M. A healable and mechanically enhanced composite with segregated conductive network structure for high-efficient electromagnetic interference shielding. *Nano-Micro Lett.* **2021**, *13*, 162.
[31] Wang, T.; Yu, W. C.; Sun, W. J.; Jia, L. C.; Gao, J. F.; Tang, J. H.; Su, H. J.; Yan, D. X.; Li, Z. M. Healable polyurethane/carbon nanotube composite with segregated structure for efficient electromagnetic interference shielding. *Compos. Sci. Technol.* **2020**, *200*, 108446.
[32] Sharif, F.; Arjmand, M.; Moud, A. A.; Sundararaj, U.; Roberts, E. P. L. Segregated hybrid poly(methyl methacrylate)/graphene/magnetite nanocomposites for electromagnetic interference shielding. *ACS Appl. Mater. Interfaces.* **2017**, *9*, 14171–14179.
[33] Tang, X. H.; Tang, Y.; Wang, Y.; Weng, Y. X.; Wang, M. Interfacial metallization in segregated poly (lactic acid)/poly (ε-caprolactone)/multi-walled carbon nanotubes composites for enhancing electromagnetic interference shielding. *Compos. Part A: Appl. Sci. Manuf.* **2020**, *139*, 106116.
[34] Wang, M.; Tang, X. H.; Cai, J. H.; Wu, H.; Shen, J. B.; Guo, S. Y. Construction, mechanism and prospective of conductive polymer composites with multiple interfaces for electromagnetic interference shielding: A review. *Carbon.* **2021**, *177*, 377–402.
[35] He, Q. M.; Tao, J. R.; Yang, Y.; Yang, D.; Zhang, K.; Wang, M. Effect surface micro-wrinkles and micro-cracks on microwave shielding performance of copper-coated carbon nanotubes/polydimethylsiloxane composites. *Carbon.* **2023**, *213*, 118216.
[36] Wang, Z. Y.; Yang, W. Z.; Liu, R.; Zhang, X. L.; Nie, H. Y.; Liu, Y. Highly stretchable graphene/polydimethylsiloxane composite lattices with tailored structure for strain-tolerant EMI shielding performance. *Compos. Sci. Technol.* **2021**, *206*, 108652.
[37] Luo, C. L.; Huang, M. L.; Sun, C.; Zhao, K. Y.; Guo, H.; Wang, M. Anisotropic electromagnetic wave shielding performance in Janus cellulose nanofiber composite films. *Mater. Today Phys.* **2024**, *44*, 101440.
[38] Li, Y.; Sun, L.; Xu, F.; Wang, S. S.; Peng, Q. Y.; Yang, Z. Y.; He, X. D.; Li, Y. B. Electromagnetic and acoustic double-shielding graphene-based metastructures. *Nanoscale.* **2019**, *11*, 1692–1699.
[39] Li, J. J.; Zhang, Y.; Li, X. F.; Chen, C. Y.; Zou, H. H.; Yi, P.; Liu, X. F.; Yu, R. H. Oriented magnetic liquid metal-filled interlocked bilayer films as multifunctional smart electromagnetic devices. *Nano Res.* **2023**, *16*, 1764–1772.
[40] Verma, S.; Dhangar, M.; Mili, M.; Bajpai, H.; Dwivedi, U.; Kumari, N.; Khan, M. A.; Bhargaw, H. N.; Hashmi, S. A. R.; Srivastava, A. K. Review on engineering designing of electromagnetic interference shielding materials using additive manufacturing. *Polym. Compos.* **2022**, *43*, 4081–4099.
[41] Pei, X. Y.; Liu, G. D.; Shao, R. Q.; Yu, R. R.; Chen, R. X.; Liu, D.; Wang, W.; Min, C. Y.; Liu, S. K.; Xu, Z. W. 3D-printing carbon nanotubes/$Ti_3C_2T_x$/chitosan composites with different arrangement structures based on ball milling for EMI shielding. *J. Appl. Polym. Sci.* **2022**, *139*, e53125.
[42] Lv, Q. N.; Tao, X. Y.; Shi, S. H.; Li, Y. J.; Chen, N. From materials to components: 3D-printed architected honeycombs toward high-performance and tunable electromagnetic interference shielding. *Compos. Part B: Eng.* **2022**, *230*, 109500.
[43] Lee, K. P. M.; Baum, T.; Shanks, R.; Daver, F. Electromagnetic interference shielding of 3D-printed graphene-polyamide-6 composites with 3D-printed morphology. *Addit. Manuf.* **2021**, *43*, 102020.
[44] Liu, G. D.; Yu, R. R.; Liu, D.; Xia, Y. H.; Pei, X. Y.; Wang, W.; Min, C. Y.; Liu, S. K.; Shao, R. Q.; Xu, Z. W. 3D-printed TiO_2–$Ti_3C_2T_x$ heterojunction/rGO/PDMS composites with gradient pore size for electromagnetic interference shielding and thermal management. *Compos. Part A: Appl. Sci. Manuf.* **2022**, *160*, 107058.
[45] Pei, X. Y.; Liu, G. D.; Shi, H. T.; Yu, R. R.; Wang, S.; Liu, S. K.; Min, C. Y.; Song, J. N.; Shao, R. Q.; Xu, Z. W. Directional electromagnetic interference shielding of asymmetric structure based on dual-needle 3D printing. *Compos. Sci. Technol.* **2023**, *233*, 109909.
[46] Ma, T. B.; Ma, H.; Ruan, K. P.; Shi, X. T.; Qiu, H.; Gao, S. Y.; Gu, J. W. Thermally conductive poly (lactic acid) composites with superior electromagnetic shielding performances via 3D printing technology. *Chin. J. Polym. Sci.* **2022**, *40*, 248–255.

[47] Dai, L.; Wang, L. Q.; Chen, B. H.; Xu, Z. T.; Wang, Z. J.; Xiao, R. Shape memory behaviors of 3D printed liquid crystal elastomers. *Soft Sci.* **2023**, *3*, 5.

[48] Wang, Y.; He, Q. M.; Gao, Y. N.; Yue, T. N.; Wang, M. Achieving remarkable enhancement on electromagnetic shielding performance in multi-walled carbon nanotube/polydimethylsiloxane composites via adding a small amount of metal micro-particles as scattering points. *Compos. Part A: Appl. Sci. Manuf.* **2022**, *162*, 107135.

[49] Rajan, A. K.; Solaman, S.; Ganesanpotti, S. Design and fabrication of layered electromagnetic interference shielding materials: A cost-effective strategy for performance prediction and efficiency tuning. *ACS Appl. Mater. Interfaces.* **2023**, *15*, 5822–5835.

[50] Cheng, R.; Wang, B.; Zeng, J. S.; Li, J. P.; Xu, J.; Gao, W. H.; Chen, K. F. Janus-inspired flexible cellulose nanofiber-assisted MXene/silver nanowire papers with fascinating mechanical properties for efficient electromagnetic interference shielding. *Carbon.* **2023**, *202*, 314–324.

[51] Yazdi, S. J. M.; Lisitski, A.; Pack, S.; Hiziroglu, H. R.; Baqersad, J. Analysis of shielding effectiveness against electromagnetic interference (EMI) for metal-coated polymeric materials. *Polymers.* **2023**, *15*, 1911.

[52] Habib, S.; Kiani, G. I.; Butt, M. F. U. A convoluted frequency selective surface for wideband communication applications. *IEEE Access.* **2019**, *7*, 65075–65082.

[53] Liao, S. Y.; Wang, X. Y.; Li, X. M.; Wan, Y. J.; Zhao, T.; Hu, Y. G.; Zhu, P. L.; Sun, R.; Wong, C. P. Flexible liquid metal/cellulose nanofiber composites film with excellent thermal reliability for highly efficient and broadband EMI shielding. *Chem. Eng. J.* **2021**, *422*, 129962.

[54] Li, T.; Li, J. Z.; Xu, Z. K.; Tian, Y. R.; Li, J. T.; Du, J. N.; Meng, F. B. Electromagnetic response of multistage-helical nano-micro conducting polymer structures and their enhanced attenuation mechanism of multiscale-chiral synergistic effect. *Small.* **2023**, *19*, 2300233.

[55] Yao, H. M.; Yang, J. P.; Li, H.; Xu, J. C.; Bi, K. Optimal design of multilayer radar absorbing materials: A simulation-optimization approach. *Adv. Compos. Hybrid Mater.* **2023**, *6*, 43.

[56] Zhou, Q.; Shi, T. T.; Xue, B.; Gu, S. Y.; Ren, W.; Ye, F.; Fan, X. M.; Du, L. F. Multi-scale integrated design and fabrication of ultra-broadband electromagnetic absorption utilizing multi-walled carbon nanotubes-based hierarchical metamaterial. *Compos. Sci. Technol.* **2023**, *232*, 109877.

[57] Bai, Y. Y.; Wang, J. J.; Lu, S. W.; Huang, Z. W.; Zhang, L.; Xu, Q. G.; Xu, S. F. Ni deposited onto MWCNTs buckypapers for improved broadband EMI shielding. *J. Mater. Sci.: Mater. Electron.* **2018**, *29*, 15034–15041.

[58] Kumar, G. S.; Vishnupriya, D.; Joshi, A.; Datar, S.; Patro, T. U. Electromagnetic interference shielding in 1–18 GHz frequency and electrical property correlations in poly(vinylidene fluoride)-multi-walled carbon nanotube composites. *Phys. Chem. Chem. Phys.* **2015**, *17*, 20347–20360.

[59] Mohan, R. R.; Varma, S. J.; Faisal, M.; Jayalekshmi, S. Polyaniline/graphene hybrid film as an effective broadband electromagnetic shield. *RSC Adv.* **2015**, *5*, 5917–5923.

[60] Fan, M. S.; Xia, X.; Li, S. H.; Zhang, R.; Wu, L.; Qu, M. J.; Tang, P.; Bin, Y. Z. Sustainable bacterial cellulose reinforced carbon nanotube buckypaper and its multifunctionality for electromagnetic interference shielding, Joule heating and humidity sensing. *Chem. Eng. J.* **2022**, *441*, 136103.

[61] Hou, C. X.; Cheng, J. Y.; Zhang, H. B.; Lu, Z. H.; Yang, X. Y.; Zheng, G. P.; Zhang, D. Q.; Cao, M. S. Biomass-derived carbon-coated WS_2 core–shell nanostructures with excellent electromagnetic absorption in C-band. *Appl. Surf. Sci.* **2022**, *577*, 151939.

[62] Akram, S.; Aziz, H.; Imran, A.; Javid, A.; Nosheen, A.; Ashraf, M.; Xue, Z. B.; Raza, M. Fabrication of silver/polyaniline/aminated graphene oxide coated textiles for electromagnetic interference shielding application within the different bands of frequency. *Synth. Met.* **2023**, *298*, 117440.

[63] Yang, X. F.; He, W. J.; Xu, Q.; Wang, H. P.; Xing, H. N.; Feng, J.; Zhu, X. H.; Li, X. H.; Zhang, J. W.; Zheng, X. L. Flexible and ultrathin GO@MXene sandwich-type multilayered film toward superior electromagnetic interference shielding in a wide gigahertz range of 3.95–18.0 GHz. *J. Alloy. Compd.* **2023**, *964*, 169338.

[64] Shukla, V.; Srivastava, S. K. Reduced graphene oxide/PdNi/poly(ethylene-co-vinyl acetate) nanocomposites for electromagnetic interference shielding. *Mater. Chem. Phys.* **2022**, *276*, 125418.

[65] Guo, Y. Q.; Wang, S. S.; Zhang, H. T.; Guo, H.; He, M. K.; Ruan, K. P.; Yu, Z.; Wang, G. S.; Qiu, H.; Gu, J. W. Consistent thermal conductivities of spring-like structured polydimethylsiloxane composites under large deformation. *Adv. Mater.* **2024**, *36*, 2404648.

[66] Ma, Y. S.; Luo, N.; Ni, Z. Y.; Guan, R. T.; Zhang, G. R.; Wang, Y.; Chen, F. Resonant cavity structural design of carbon-based intrinsic metamaterial absorbers for broadening the effective absorption bandwidth. *Chem. Eng. J.* **2024**, *500*, 157508.

[67] Wang, M. Biodegradable polymer-based nanocomposite foams for electromagnetic interference shielding. In *Porous Nanocomposites for Electromagnetic Interference Shielding*. Thomas, S.; Paoloni, C.; Pai, A. R., Eds.; Woodhead Publishing: Cambridge, 2024; pp 179–219.

[68] Hou, X.; Feng, X. R.; Jiang, K.; Zheng, Y. C.; Liu, J. T.; Wang, M. Recent progress in smart electromagnetic interference shielding materials. *J. Mater. Sci. Technol.* **2024**, *186*, 256–271.

[69] Zhang, Y. L.; Ruan, K. P.; Zhou, K.; Gu, J. W. Controlled distributed $Ti_3C_2T_x$ hollow microspheres on thermally conductive polyimide composite films for excellent electromagnetic interference shielding. *Adv. Mater.* **2023**, *35*, 2211642.